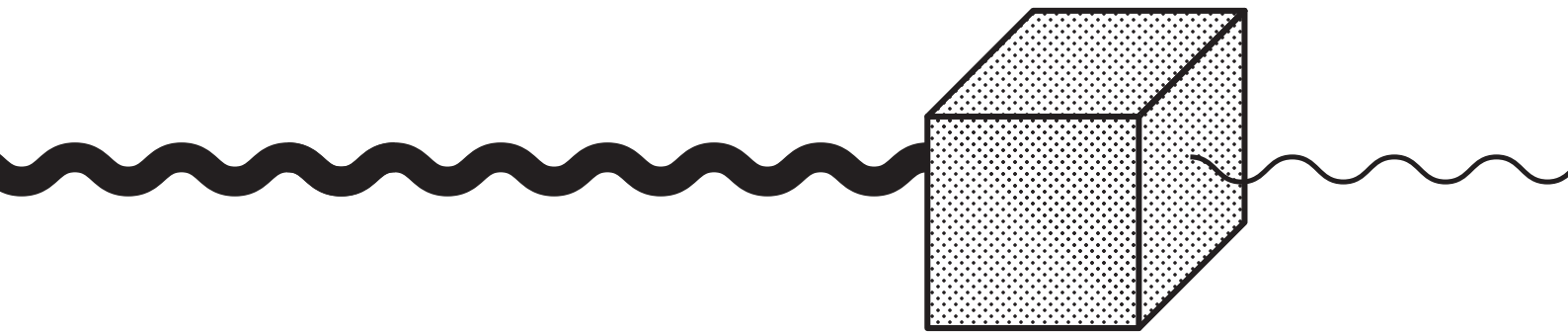Technische Universität Dortmund

Fakultät Physik

Lehrstuhl für Experimentelle Physik III

Computed tomography with gamma radiation and Arduino microcontrollers

Bachelorarbeit

zum Erwerb des Bachelor of Science der Physik

Florian Gubernator

vorgelegt am 25. Februar 2014

1. Gutachter   : Prof. Dr. Dieter Suter

2. Gutachterin : Dr. Bärbel Siegmann

Datum des Einreichens der Arbeit: 25. Februar 2014

Abstract

A set-up to create tomographic images of small samples was built. With the aid of an Arduino microcontroller and computers the gathering of data and the image reconstruction of a cross section can be performed via filtered back-projection. This allow for the collection of images that resolve structures with diameters of about $1\,\text{mm}$. It may be possible for students to conduct this experiment in a simplified form as part of their laboratory practical course.

Kurzfassung

Es wurde ein Aufbau erstellt, in dem eine kleine Probe tomografiert werden kann. Mithilfe eines Arduino Mikrocontrollers und Computern ist die Aufnahme eines Schnittbildes und die Bildauswertung mittels gefilterter Rückprojektion möglich.

Der Versuch liefert Bilder, die Strukturen von einem Durchmesser von etwa $1\,\text{mm}$ auflösen können.

In der Zukunft ist es vielleicht möglich, das Experiment in aufbereiteter und vereinfachter Form im Praktikum als Versuch für Studierende durchzuführen.

Contents

Introduction

Computed tomography is a method of resolving cross-sections of objects with the computer-aided analysis of density data. The data are obtained, for example, by exposure with X-rays. Computed tomography is applied in medicine as well as scientific research.

The principle of computed tomography (CT) was first proven with a working prototype in 1969 by Sir Godfrey Hounsfield at Electric and Musical Industries in Hayes, Middlesex (GB) and, during the 1970s, the principal clinical tests and applications were developed [Buz08]. Today X-ray CT is a widely used tool in medical diagnostics with a focus on trauma (accident diagnostics), the head, lungs and the musculoskeletal system. Additionally other forms of tomography have been developed, such as magnetic resonance imaging, positron emission tomography and others, utilising different physical phenomena.

In this work, 2D tomography using pencil geometry is discussed. In medical applications today, the most widely used methods are 3D imaging systems using fan-beam geometry. [Buz08].

Using readily available components and almost exclusively custom, self-written software a set-up was built with results of the imaging process able to resolve structures with a size of $1\,\mathrm{mm}$.

In the first part of this thesis, the physical foundations and fundamental concepts of CT are presented. This will be followed by an extensive account of the implementation, the used methods of simulation and the results. Lastly some suggestions on the improvement and educational values of the set-up will be made.

This work will put emphasis on the mathematical aspects of the image reconstruction and absorption phenomena, while practical instructions on the operation of the experiment and more extensive examples of the source code and the computational insights of the reconstruction process can be found in [Lem14].

A digital version of this work, as well as the developed software, can be found at `http://projekte.free.de/ct`.

1   Conceptual basis

Computed tomography offers the possibility of a non-invasive imaging of structures inside of bodies without the superimposing effects of traditional radiography. With CT imaging, the reconstruction of the attenuation values of a slice in the body is possible, as the attenuation of penetrating radiation is measured.
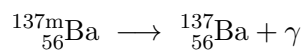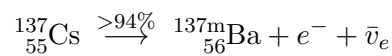
1.1   Physical foundations

The underlying principle of X-ray and gamma ray tomography is the observation of the absorption coefficient of different materials through the measurement of the attenuation of radiation. For a precise measurement the source of radiation needs a constant emission rate and the detector should have well defined response to the radiation received.

^{137}Cs was used as a source emitting gamma radiation and a scintillation counter with a NaI crystal for the detection.

1.1.1   Gamma radiation

Gamma radiation is electromagnetic radiation of very high frequencies. The used radiation source is ^{137}Cs, which decays with a probability of $> 94\%$ into the nuclear isomer $^{137\mathrm{m}}$Ba that returns to the ground state ^{137}Ba and emits gamma rays at an energy of $662\,\mathrm{keV}$.

$$^{137}_{55}\mathrm{Cs} \xrightarrow{>94\%} {}^{137\mathrm{m}}_{56}\mathrm{Ba} + e^- + \bar{v}_e$$

$$^{137\mathrm{m}}_{56}\mathrm{Ba} \longrightarrow {}^{137}_{56}\mathrm{Ba} + \gamma$$

This decay chain progresses at a sufficiently constant rate (see section 2.2) as ^{137}Cs has a half-life of $(11018.3 \pm 9.5)\,\mathrm{d}$, which is also more than adequate for a time constant emission [UHSC].

Passing through matter, gamma rays interact with the material in various ways. Depending on the energy of the gamma particles, different effects play a more important role. The primary effects of interaction that are of interest in the set-up employed are

2

Compton scattering and the photoelectric effect, as they contribute predominantly to the attenuation coefficient at the energies of the gamma photons emitted by the caesium source and explain the principle of the scintillation counter.

Photoelectric absorption is an effect in which a photon is terminated by transmitting its complete energy $h \cdot \nu$ to *one* photo electron. By this the electron is freed from the forces holding it in the material and thereby it is emitted (figure 1.1 (a)).

The **Compton effect** is an interaction in which the gamma photon transmits energy to a (nearly free) electron, transmitting kinetic energy and changing the path of movement itself, similar to an elastic collision (figure 1.1 (b)) [Dem05].


(a) photoelectric effect   **(b)** inelastic Compton scattering
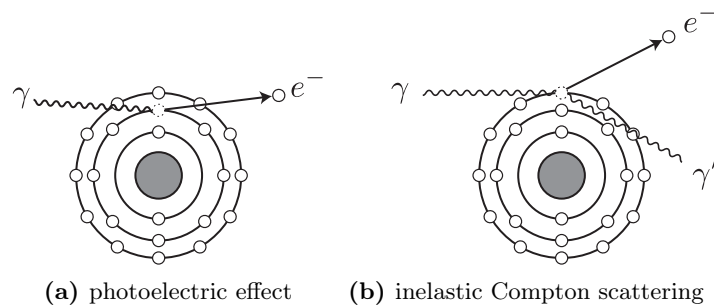
Figure 1.1: Photoelectric effect and Compton scattering [Buz08]

The spectrum of the ^{137}Cs source shows a relatively sharp spike at $662\,\text{keV}$ and a broad range at lower energy levels called the Compton edge. This is caused by scattering and reflection in the sample and in the scintillation counter, because the Compton effect not only produces an electron with $E_{kin} < h \cdot \nu_\gamma$, but also a scattered gamma quant with the energy $h \cdot \nu' < h \cdot \nu_\gamma$. Therefore the spectrum shows a narrow maximum at $E_{kin} = h \cdot \nu_\gamma$ called the 'photo peak' and a broader distribution at $E < E_{kin}$ that corresponds to the energy distribution of the Compton electrons [Dem10]. The spectrum (figure 1.2) that was recorded with the source exhibits these properties.
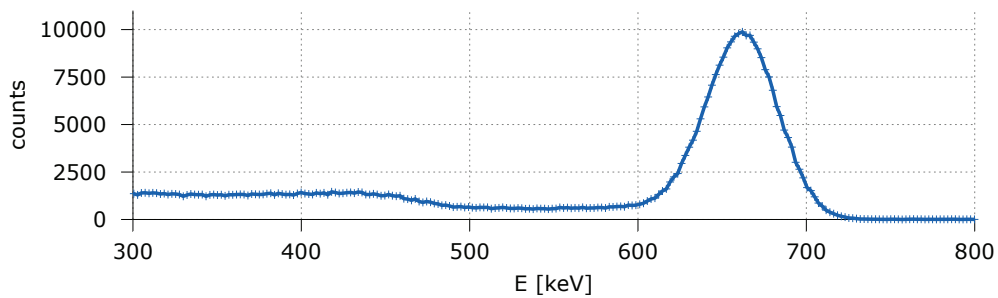
Figure 1.2: Measurement of the energy spectrum of the ^{137}Cs source used in the experiment

Figure 1.3 shows the curve of the mass attenuation coefficient for iron and Delrin (polyoxymethylene) in regard to the energy of the gamma quant. In the range of $\approx 700 keV$ as used in the experiment gamma rays interact primarily through Compton scattering and the photoelectric effect, and the mass attenuation coefficients μ/ρ are comparable.
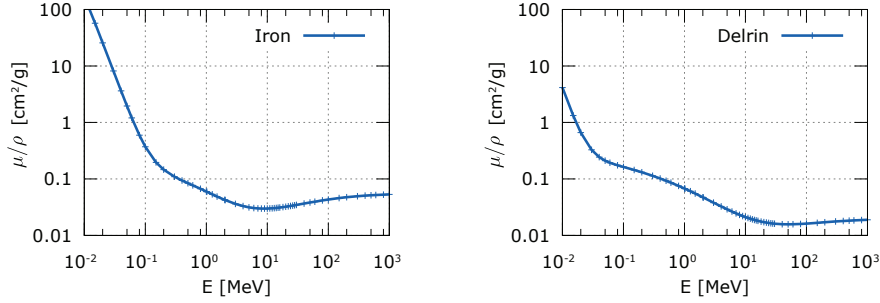
Figure 1.3: Graph of the mass attenuation coefficient $\frac{\mu}{\rho}$ versus incident photon energy for iron and Delrin with data by [BHS+10]

1.1.2 Attenuation of radiation

The attenuation of a material is often summarised by a single attenuation coefficient μ. The intensity of the penetrating ray is then given by Beer's Law in regard to the thickness η by

$$I(\eta) = I_0 \cdot e^{-\mu\eta}. \tag{1.1}$$

This attenuation coefficient μ will be subject to the considerations and the value finally displayed in the resulting images.

1.1.3 Measurement of gamma radiation with a scintillation counter

The gamma particles, that have passed through the object, can be counted with a scintillation counter.

A scintillation counter is an instrument for detecting ionizing radiation of low intensities and was used in this set-up to count the radiation events. While photons carry no charge, they can be indirectly ionizing via the photoelectric or Compton effect. In a scintillation counter the investigated particles produce a flash of light by exciting atoms or molecules in the scintillator material. These are made observable by a photo multiplier; a fraction of the photons emitted reach the cathode of the photomultiplier, where
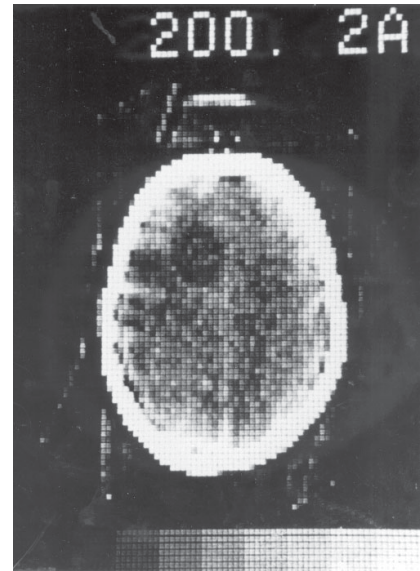
they cause the emission of an electron via the photoelectric effect, which is accelerated in an electric field and multiplied through several stimulations of electrons at metal surfaces (dynodes). As a result, this produces a voltage pulse proportional to the energy E_{kin} of the studied particle [Dem10]. This pulse can then be evaluated by a peak height analyser and transmitted to a computer for further processing.

As monoenergetic radiation is ideally measured, a cut off with a threshold right under the peak is implemented and merely the count of events is considered, as only these pulses will be counted by the electronic setup.

1.2 Technical basis and scanner geometries

For a tomographic image the object has to be scanned in two dimensions, by taking a lot of single 1D measurements as opposed to the method of radiography, where the image is generated by projecting a beam onto a 2D detector (such as chemical film or digital sensor). This requires either the source and/or detector(s) to move around the object or for the object to move between the parts of the measuring system. In modern medical applications, a combination of the two is used [Buz08].

The first generation of CT-scanners employed a technique where the source and the detector perform a translation and a rotation while maintaining their relative positions. In this manner, one data point at a time is collected. This of course prolongs the time for one image significantly and consequently the first CT-scanner of this kind took 9 days to complete one

Figure 1.4: First patient image scanned on the prototype EMI scanner at Atkinson Morley's Hospital on 1st October 1971 [Bec06]

series of measurements [Dös99]. Later generations used an array of detectors arranged in a line, reducing the duration of the reading. When the span of the detector array is wide enough so that the detected rays cover the whole width of the object, it is possible even to do without the translation, reducing the movement involved to just a rotation. It is then possible to refrain from a translation in the plane of the image and instead

to perform one perpendicular to the plane, to record multiple slices from which a 3D representation can be retrieved.

The fourth generation CT scanner has a complete ring of detectors, making their movement obsolete, and rotating only the source of radiation, thereby allowing for more compact appliances.

An apparatus of the kind of the first CT-scanner was used in the experiment, as an array of detectors was not a feasible option, while a single beam measurement is. This of course requires a much longer time compared to the other models, as only one projection at a time is measured.

1.3 Mathematical basis

The data points obtained in the measurements performed in the experiment are in principle the Radon transforms on the density function of the studied object [Buz08]. The image can be reconstructed from the obtained values by different methods. The most intuitive is a solution of the wanted matrix of grey values by solving the over-defined set of equations with a least squares fit. While this method is relatively simple in terms of the mathematics involved, it is also very computationally expensive for larger images. For a very high number of data points, an inverse Fourier transform can be used to reconstruct the image.

Another widely used method for the reconstruction of the image that can also use data that is not as dense is the so called back projection, which is able to easily reconstruct the image, but produces a lot of artefacts in the reconstructed image making it appear smeared. To counteract this problem, a so called filtered back projection is introduced with the capability to eliminate some of the artefacts. The filtered back projection is itself one kind of inverse Radon transform [Buz08].

A comprehensive account of the mathematical methods of a filtered back projection can more than fill a thesis itself. Therefore many topics, albeit interesting, like problems in discrete image and signal processing, discrete and fast Fourier transforms and others are omitted in favor of a stringent derivation of the methods used and needed for the analysis and a short complement regarding the methodology of the filtered back projection using Fourier transforms. The following explanation is an adaptation of the deliberations in

"Computed Tomography - From Photon Statistics to Modern Cone-Beam CT" [Buz08], in some instances slightly modified to be more readable, reduced to the parts relevant to the measurements and supplemented by examples of the actual data. We will discuss CT using pencil geometry as opposed to fan beam geometry, which is widely used in CT applications today (figure 1.5 illustrates the difference).

(a) First generation CT   (b) Second generation CT
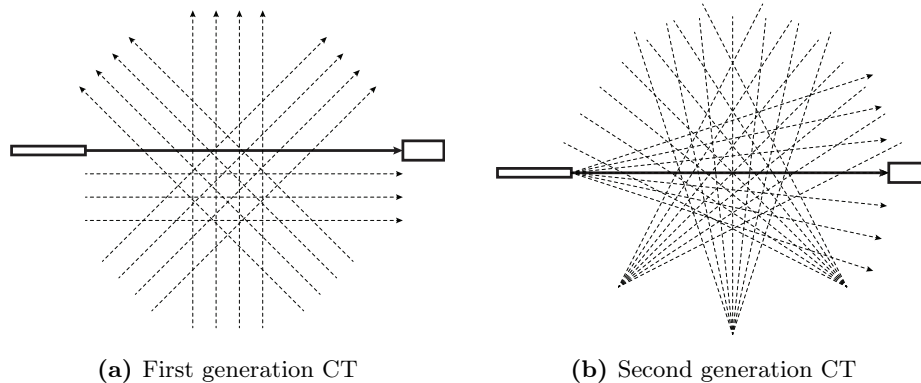
Figure 1.5: Schematic drawing of the beams measured in a CT-scanner of the first and second kind
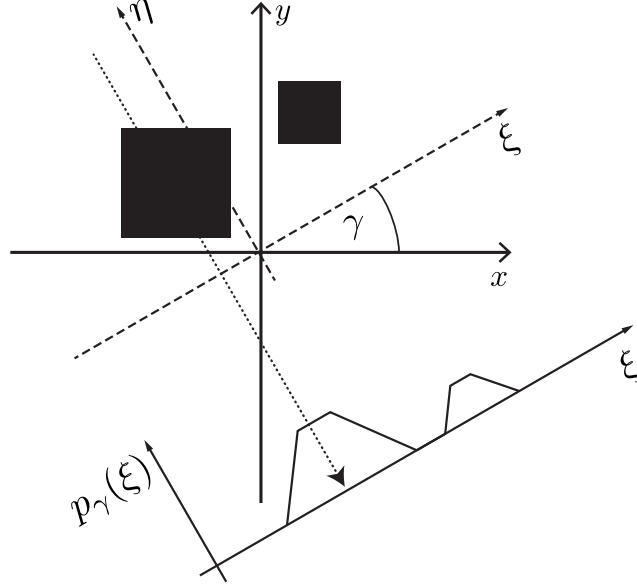
1.3.1 Radon transform

In 1917 Johann Radon published a method for a projection and reconstruction of a 2D plane. About 50 years later, his article gained unexpected relevance in computed tomography, as it lays the theoretical basis for reconstruction of 2D functions by virtue of their projections along straight lines.

A Radon transform is an integral transform, constituted by integrals taken over a density function $f(x, y)$ in straight lines. This process yields a projection function $p_\gamma(\xi)$ [Buz08]. Radon himself proved in 1917 that a Radon transform is reversible for an unlimited number of data points, that is, a continuos integration [Rad17].

The function of the absorption coefficient shall be called $f(x, y)$ in cartesian coordinates and $\mu(\xi, \eta)$ in a coordinate system rotated by an angle γ. Integration over the function $\mu(\xi, \eta)$ with a fixed length s of the integration gives the projection

$$p_\gamma(\xi) = \int_{s_1}^{s_2} \mu(\xi, \eta) \, \mathrm{d}\eta. \tag{1.2}$$

An example result for a $p_\gamma(\xi)$ is given in figure 1.6.

7

Figure 1.6: The Radon transform and the (ξ, η) coordinate system

The (ξ, η)-system can be understood as the measurement apparatus performing a translation movement ξ along a axis tilted by γ. The static coordinate system (x, y) can be transformed into the system (ξ, η) of the measurement fixture by projecting the x, y values on the unit vectors

$$\vec{e}_\xi = \begin{pmatrix} \cos(\gamma) \\ \sin(\gamma) \end{pmatrix} \qquad \vec{e}_\eta = \begin{pmatrix} -\sin(\gamma) \\ \cos(\gamma) \end{pmatrix} \tag{1.3}$$

of the (ξ, η) system, yielding

$$\xi = (x, y) \cdot \vec{e}_\xi = x \cos(\gamma) + y \sin(\gamma)$$
$$\eta = (x, y) \cdot \vec{e}_\eta = -x \sin(\gamma) + y \cos(\gamma). \tag{1.4}$$

The function $f(x, y)$ can now also be expressed in the (ξ, η) system and is called $\mu(\xi, \eta)$. It is defined by

$$f(x, y) = \mu(\xi(x, y), \eta(x, y)) = \mu((x, y) \cdot \vec{e}_\xi, (x, y) \cdot \vec{e}_\eta)$$
$$= \mu(\mathbf{r} \cdot \vec{e}_\xi, \mathbf{r} \cdot \vec{e}_\eta) \tag{1.5}$$

with $\mathbf{r} = (x, y)^{\mathrm{T}}$.

The Radon transform is now, as given earlier, a summation along a straight line

through the two-dimensional space (x, y), or in other words, a convolution of $f(x, y)$ along the delta function along a line $\mathbf{L}$. This line is composed of all points in (x, y) corresponding to the same value of ξ in the (ξ, η)-system. $\mathbf{L}$ can then be replaced by $(\mathbf{r}^{\mathrm{T}} \vec{e}_\xi = \xi)$, thus

$$
\begin{aligned}
f * \delta(\mathbf{L}) &= \int f(\mathbf{r}) \delta((\mathbf{r}^{\mathrm{T}} \vec{e}_\xi) - \xi) \, \mathrm{d}\mathbf{r} \\
&= \int_{-\infty}^{\infty} \int_{-\infty}^{\infty} f(x, y) \delta(x \cos(\gamma) + y \sin(\gamma) - \xi) \, \mathrm{d}x \, \mathrm{d}y \qquad (1.6) \\
&= p_\gamma(\xi)
\end{aligned}
$$

Which can be expressed compactly as

$$
f(x, y) \overset{\mathcal{R}_2}{\circ\!\!-\!\!\!-\!\!\bullet} f * \delta(\mathbf{L}) = p_\gamma(\xi) \qquad \text{or} \qquad p_\gamma(\xi) = \mathcal{R}_2\{f(x, y)\}. \qquad (1.7)
$$
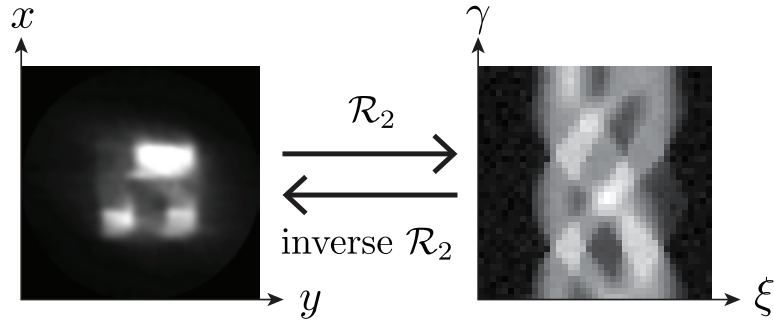
Figure 1.7: Illustration of the Radon space and reconstructed images of the measurements

Figure 1.7 shows the values of two measurement in the Radon space, thereby presenting the whole of the obtained information, and the respective images, reconstructed by the inverse $\mathcal{R}_2$ transform.

1.3.2 Fourier slice theorem

The goal is now to reverse this Radon transform to obtain the original values $f(x, y)$ or $\mu(\eta, \xi)$. The Fourier slice theorem offers a connection between the two.

Theorem 1 *Fourier slice theorem*
Let $f(x, y)$ be a function and $F(u, v)$ the 2D Fourier transform of f

$$
f(x, y) \overset{\text{2D FT}}{\circ\!\!-\!\!\!-\!\!\bullet} F(u, v). \qquad (1.8)
$$

Furthermore let $p_\gamma(\xi)$ be the Radon projection of $f(x,y)$ and $P_\gamma(w)$ the 1D Fourier transform of $p_\gamma(\xi)$

$$p_\gamma(\xi) \overset{\text{1D FT}}{\circ\!\!\!-\!\!\!-\!\!\!\bullet} P_\gamma(w). \tag{1.9}$$

Then P_γ gives the values of $F(u,v)$ on a radial ray to the angle of γ.[Dös99]

For an angle $\gamma = 0$ the projection is

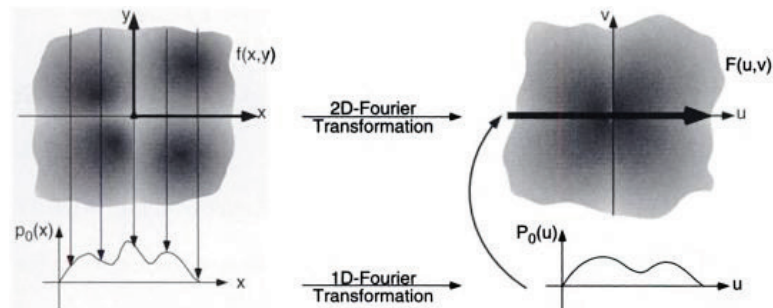$$p_\gamma(\xi) = p_0(x) = \int_{-\infty}^{\infty} f(x,y)\, \mathrm{d}y \tag{1.10}$$

and the 1D Fourier transform is then (j representing the imaginary unit)

$$P_0(u) = \int_{-\infty}^{\infty} p_0(x) \cdot e^{-j2\pi ux}\, \mathrm{d}x, \tag{1.11}$$

which can be also expressed as

$$
\begin{aligned}
P_0(u) &= \int_{-\infty}^{\infty} \left[\int_{-\infty}^{\infty} f(x,y)\, \mathrm{d}y \right] \cdot e^{-j2\pi ux}\, \mathrm{d}x \\
&= \int_{-\infty}^{\infty} \int_{-\infty}^{\infty} f(x,y) \cdot e^{-j2\pi(u\cdot x + 0\cdot y)}\, \mathrm{d}x\, \mathrm{d}y \\
&= F(u,0)
\end{aligned}
$$

when the 2D Fourier transform of f is $f(0,y) \overset{\text{2D FT}}{\circ\!\!\!-\!\!\!-\!\!\!\bullet} F(u,0)$. Figure 1.8 shows a schematic representation of the Fourier slice theorem for a single angle $\gamma = 0$.

Figure 1.8: Fourier slice theorem for $\gamma = 0$

10

For angles different from $\gamma = 0$ this can be expanded, as a Fourier transform along a different line through the origin gives a corresponding line so that

$$P_\gamma(u) = F_{\text{polar}}(u, \gamma) \tag{1.12}$$

in polar coordinates.

The transformation of the coordinates between F_{polar} and F can be easily produced by

$$F(u\cos(\gamma), u\sin(\gamma)) = F_{\text{polar}}(u, \gamma). \tag{1.13}$$

As F_{polar} is $P_\gamma(u)$ by the Fourier slice theorem,

$$F(u\cos(\gamma), u\sin(\gamma)) = P(u, \gamma) = P_\gamma(u). \tag{1.14}$$

This is an important result, as it in theory gives a possibility to reconstruct the image from the Radon space using Fourier transforms, which are also well implemented in software (e.g. a 'fast Fourier transform'). Today however a filtered back projection is used for most applications.
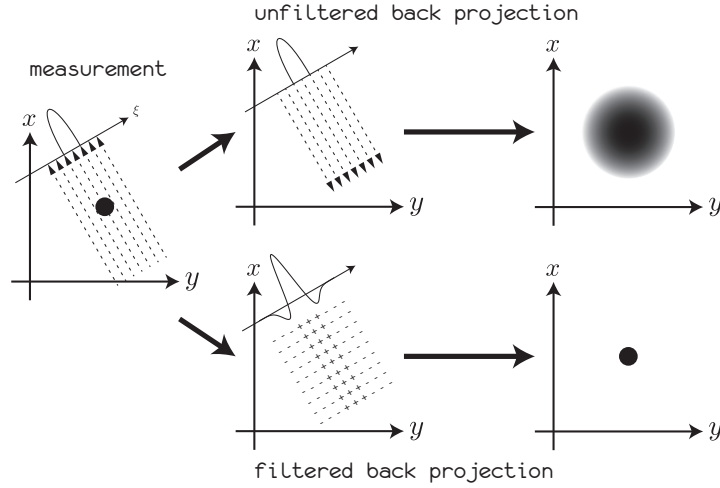
1.3.3 Filtered back projection

A more naive approach to retrieving the original values of $f(x, y)$ is to perform a back projection by summation over the projected values of every point

$$g(x, y) = \int_0^\pi p_\gamma(\xi) \, \mathrm{d}\gamma = \int_0^\pi p_\gamma(x\cos(\gamma) + y\sin(\gamma)) \, \mathrm{d}\gamma. \tag{1.15}$$

This however produces a lot of artefacts as the values are smeared across the image. It is immediately clear why the simple back projection can not offer correct results: Every dot in the plane of $f(x, y)$ produces a line on $g(x, y)$ for every angle γ without the possibility of correction, as every element of the sum is non-negative (since $p_\gamma \geq 0$). These effects are depicted in figure 1.9, which compares the unfiltered to the filtered back projection. Hence it is necessary to counter this effect. This can be done by applying a filter on the projection functions.

In practice, this filtering function has to be determined empirically. Two different methods of reconstruction were used.

Figure 1.9: Unfiltered and filtered back projection [Dös99]

At first a filter was applied over a discrete set of measured projections $\mathbf{p} = \{p_\gamma(0), \ldots, p_\gamma(n-1)\}$ that are measured with the same angle to get

$$\mathbf{p}_{\text{filtered}}(i) = \mathbf{p}(i) \quad - \sum_{\substack{0 < k < n-1 \\ k \neq i}} \frac{1}{(|k - i| \cdot a)^2} \cdot \mathbf{p}(k) \tag{1.16}$$

For the projection the algorithm then interpolates between the values of $\mathbf{p}_{\text{filtered}}$ for the translation of the image point projected on the ξ axis (see figure 1.11).

The second method employed allowed for a set of data points that is not as well known beforehand, as there are not always exactly 180° of rotation available or a translation equally wide from the centre of rotation – as the first program required. Therefore for every pixel $f_D(x, y)$ every data point in $\{p_0, \ldots, p_{n-1}\}$ is filtered by a custom function $h(d)$ and projected on f_D.

While there is no direct interpolation performed in this method, the used filter function $h(d)$ can be viewed as a convolution of an interpolating function i(d) and a filter function $\tilde{h}(d)$, that does not have to be known explicitly. The interpolating function is similar to

$$i(d) \begin{cases} 1 - |x| & \text{for } -1 < x < 1 \\ 0 & \text{else} \end{cases} \tag{1.17}$$

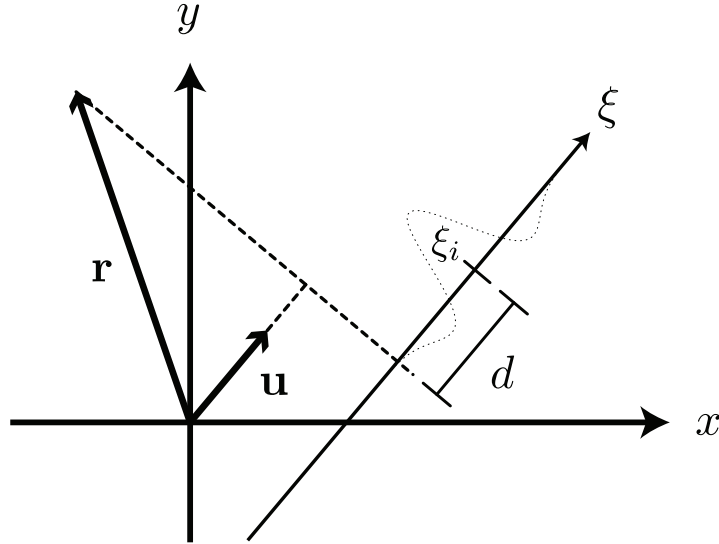The convolution $i(d) * \tilde{h}(d) = h(d)$ is illustrated in figure 1.10.
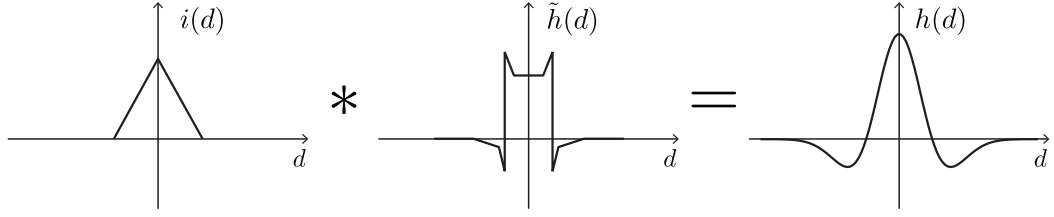
Figure 1.10: Convolution of the interpolating function with a filter function

With this the value of every pixel can now be expressed as

$$f_D(x, y) = \sum_{i=0}^{n} p_i \cdot h(d) \tag{1.18}$$

with the distance d of the pixel at $\mathbf{r}$ to the point of the measurement in terms of ξ is determined by an orthogonal projection (illustrated in figure 1.11).

**Figure 1.11:** Projection of the point (x, y) on the ξ-axis

$$d = \frac{1}{l_{\text{res}}} (\mathbf{u}^T \cdot \mathbf{r} - \xi_i) \text{ and } \mathbf{u} = \begin{pmatrix} \cos(\gamma_i) \\ \sin(\gamma_i) \end{pmatrix} \tag{1.19}$$

l_{res} being the output resolution, and $\mathbf{u}$ the unit vector of the line of movement ξ (as illustrated in figure 1.11).

13

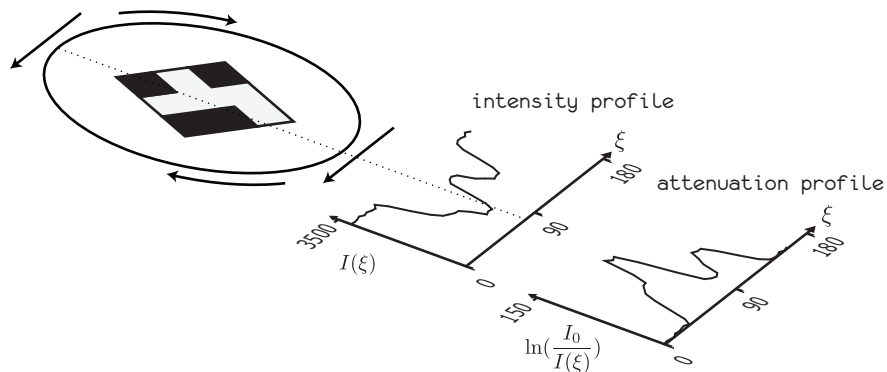The filter (figure 1.12) ultimately used was

$$h(d) = \exp\{-d^2\} \cdot (1 - (d \cdot k)^2) \tag{1.20}$$

with usable values of $1.0 < k < 1.5$ (see [Lem14] for the implementation). This filter was derived through empirical means (as is usually done, see earlier).
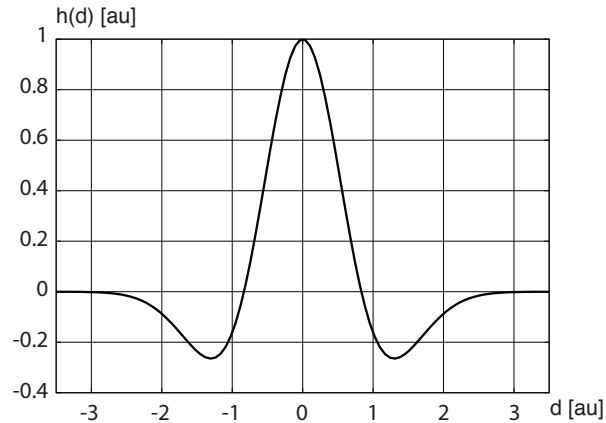
Figure 1.12: Filter with $k = 1.2$

### 1.3.4 Data processing and image generation

Figure 1.13: Processing of collected data [Klo07]

For the analysis of the obtained counts the data has to be adapted to represent attenuation values rather than the intensity of the measured beam. This conversion is illustrated in figure 1.13. The intensity of the radiation has to be converted to an attenuation profile by transforming Beer's Law (1.1) to yield the attenuation values p_γ described in (1.2)

$$p_\gamma(\xi) = \int \mu \, d\eta = \log\left(\frac{I_0}{I(\xi)}\right). \tag{1.21}$$

2 Implementation

For the experiment, mechanical parts, a shielded beam bath and detector, electronics for controls and recording, and software have to be used to create a visual cross section of the object. The set-up can be seen photographed in figure 2.1, while figure B.1 in Appendix B illustrates the schematic set-up of the experiment.
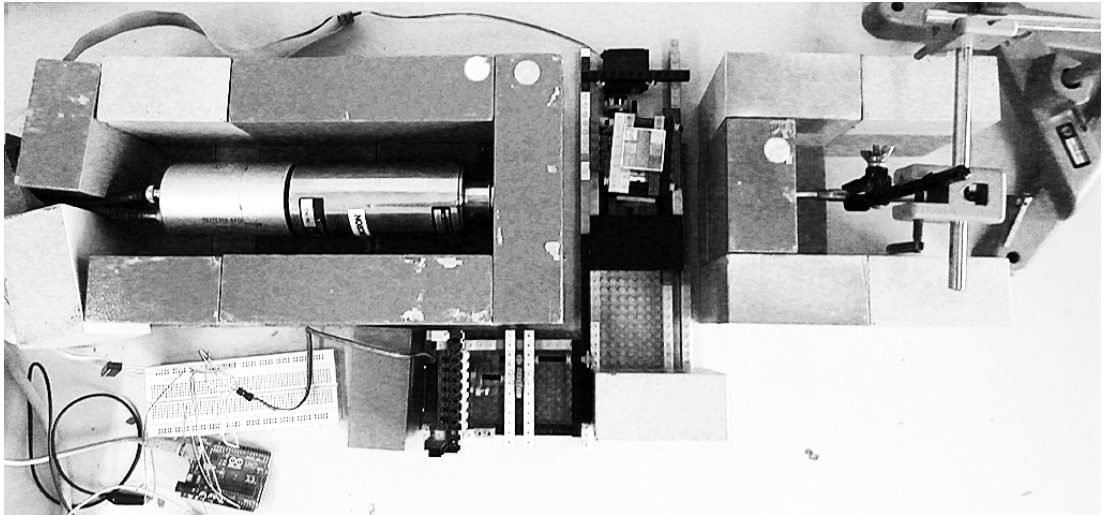
Figure 2.1: Set-up of the experiment

2.1 Mechanical implementation

To obtain the data necessary for an image reconstruction, the beam path relative to the sample has to conduct movements in two dimensions. The scintillation counter and the source along with the shielding are hard to move, while the sample is not. Along with the motor and transmission for the rotation movement the sample is therefore mounted on a sled passing through the lead sheaths of the source and the scintillation counter. This is implemented using Lego technic parts. The motors are standard servo motors. They can be actuated in 180 discrete steps performing a movement of 180°.

The rotation is executed by driving a large gear on which the object is mounted with a smaller one, mounted in a 90° angle. Via this transmission a complete rotation of the motor results in a 200° rotation of the object. For this dilation the data processing will later account. The translation is performed by a gear mounted on the second servo via another transmission that moves the sled via a toothed bar. This allows for a movement

of about 4,5 cm and effectively restricts the size of representable objects. This makes the theoretical minimal distance the sled can be moved $\frac{45}{180}$ mm $= 0,25$ mm. The sled was found to have a tendency to stick to the guide rails and moving only after several steps of the servo motor or in unpredictable step widths. To rectify this, the sled would first be moved 5 mm ahead of its target and then be pulled back to set a position. This approach increased the precision dramatically, allowing for an effective step width of about 1 mm.

2.2 Source, optical beam path and detector

A measurement to determine the source output was performed. Over a measuring period of >88 h the counts were monitored in 120 s intervals (as in the measurement of a sample) and 2650 data points were collected without an object in the beam path. The count rate was

$$N = (3139 \pm 39) \, \text{counts/minute} \tag{2.1}$$

For a single measurement a statistical error is to be expected

$$\sigma = \sqrt{N} \tag{2.2}$$

from the statistical deviations of the Poisson distribution of radioactive decay [Gup12]. For a measurement with a length of 60 s this means an error of 1.78 %; for 120 s an error of 1.26 %.

Lead shielding around the scintillation counter and the source suppress background radiation and lead apertures shape the radiation of the source to a usable beam.

A measurement to determine the background radiation recieved by the scintillation counter was conducted over a measuring period of 50 h. The counts were monitored in 120 s intervals (as in the measurement of a sample) and 1501 data points were collected without the ^{137}Cs-source in place and had a count rate of

$$N = (43 \pm 4.70) \, \text{counts/minute} \tag{2.3}$$

with this background noise of 1.37 % the signal to noise ratio is adequate.

Figure 2.2 illustrates the focusing of the beam path and the used shielding. If no scattering occurred in the sample, the beam had a theoretical diameter of $3\,\text{mm}$ throughout its path.
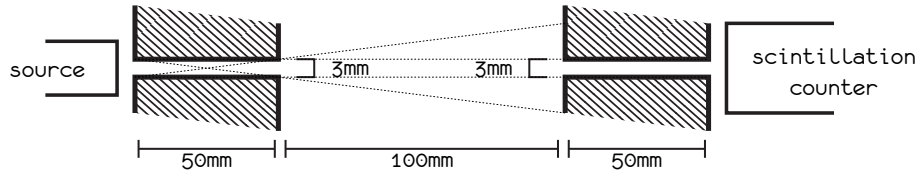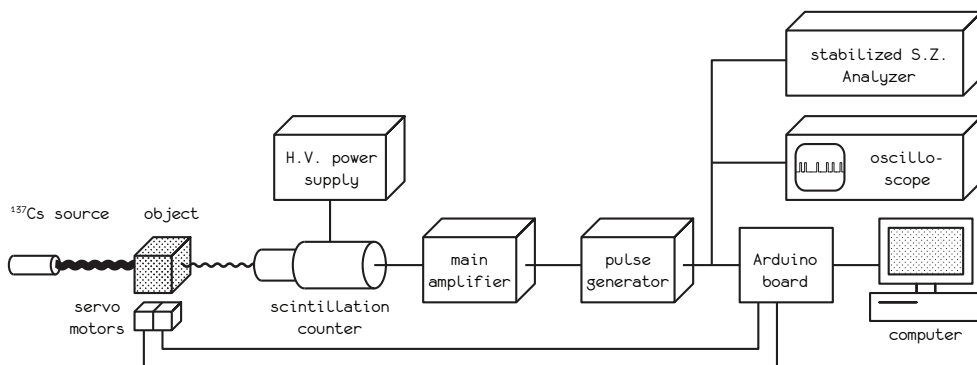

Figure 2.2: Schematic drawing of the beam path

Simple tunnels in lead blocks to narrow the radiation to a beam were used. This means that the beam has a diameter of $9\,\text{mm}$ at the object center. Photons in this wider path can scatter and also reach the counter, which can impair the measurement by adulterating the counts, while only photons traveling in a path of the $3\,\text{mm}$ wide apertures can reach the scintillation counter directly. This is why an additional shield in front of the scintillation counter is used to minimize this effect.

A lead sheath with a width of $50\,\text{mm}$ is placed around the scintillation counter. This gives a very good shielding from background noise reducing the events by roughly a factor of 1000 to $\approx 1\,\text{count/s}$.

2.3 Control electronics

The experiment electronics can be grouped in three stages: the measurement, the signal processing and the monitoring.

Figure 2.3: Schematic drawing of the electronic components

The object is irradiated by the radioactive source with the scintillation counter detecting the gamma rays. In the signal processing the voltage pulses are processed by

an amplifier and a pulse generator, so they can be detected by the Arduino board. The output is then monitored by a scintillation analyser, an oscilloscope and collected by a computer for image reconstruction. The scintillation analyser and oscilloscope have been brought into place during the development of the set-up to check the correct functioning of the counting procedures performed by the Arduino board. Section 2.4 will provide a more detailed look at the different stages of the signal.
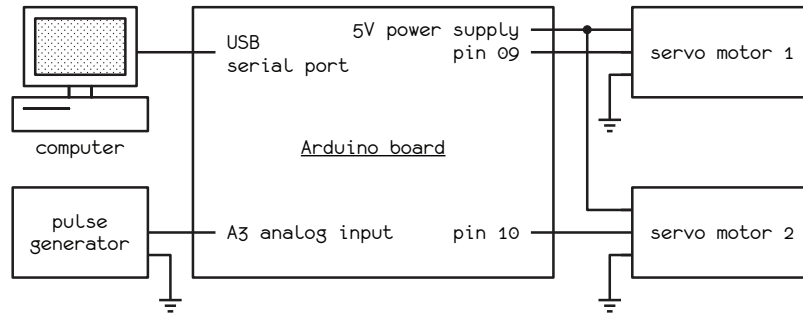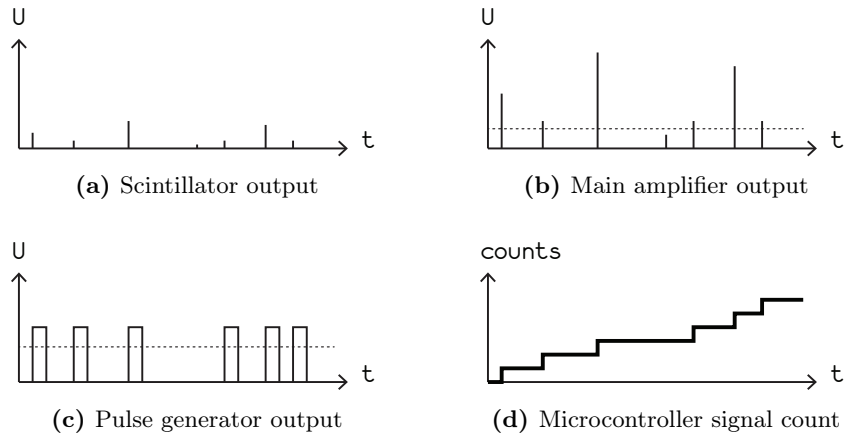

Figure 2.4: Schematic drawing of the circuitry of the Arduino microcontroller

As can be seen in figures 2.3 and 2.4, the Arduino board is a central component in the set-up as it both aggregates and transmits the events of the scintillation counter and controls the mechanical components. An Arduino Uno board is "a microcontroller board based on the ATmega328 [. . .]. It has 14 digital input/output pins (of which 6 can be used as PWM outputs), 6 analog inputs, a 16 MHz ceramic resonator, a USB connection, a power jack, an ICSP header, and a reset button." [Ard14]. It has the built-in capabilities of analog signal input and libraries for the control of servo motors. These features are controlled by programming the micro controller using Processing and the provided libraries and compilers. The source code for the Arduino board can be found in listing A.1 in Appendix A.

2.4   Signal processing

As the pulses by the scintillation counter (figure 2.5 (a)) are too short to be counted by the Arduino board directly they are passed through some electronic components to make the signal usable. The signal is amplified so that most of the pulses pass the threshold of the pulse generator (2.5 (b)). The pulse generator then produces pulses of a length of $100\,\mu\text{s}$ and a height of $3\,\text{V}$ (2.5 (c)). The Arduino board counts these

(a) Scintillator output   **(b)** Main amplifier output

(c) Pulse generator output   **(d)** Microcontroller signal count

Figure 2.5: Schematic drawing of the signal at different stages of the signal processing

pulses with a positive slope triggering at about $2/3$ of the height of a pulse by the pulse generator (2.5 (d)).

2.5 Data processing and image generation

The measured intensities are transmitted to the computer by the Arduino board via a serial connection where they are stored in a serial monitor application in CSV (comma separated values) and retrieved by copying the contents to a text file. To generate the image they then are adapted as described in section 1.3.4 by the program responsible for the image generation.

The image is generated as described earlier by calculating the reconstructed values of every single pixel in the output image. For the actual output the resulting grey values have to be mapped to luminosity values of $0-255$ to be stored in a lossless image format (png). This is implemented by a linear representation ranging from the minimum to the maximum of the calculated values.

The image generation itself is performed by an application written in the dynamic, object-oriented, high-level language Ruby. It can be started via command line specifying several parameters like `<input file>`, `<output resolution>` and a `<comment>`. Along with the output image a log file is stored documenting these values as well as the amount of data points and the used filter to make it easier to later identify the images and retrace the reconstruction process. The usage is described more extensively in [Lem14].

3 Simulation and tests

To test the image reconstruction algorithm we developed a piece of software for creating simulated measurement data. This was done by 'forward calculating' the projection that was later to be reversed.

The goals were to tune the algorithm by varying different parameters and the filter function with the knowledge of the ideal reconstruction. Apart from that the simulation offered the possibility to test the algorithms error proneness and resolution capacity.

The simulation is written in the Processing language. It has the capability of reading input images and simulating a Radon transform on the grey values and thus the attenuation of a gamma ray. After some consideration this was done by running a pointer along a constructed ray and summing the grey values of the nearest neighboring pixels.

Figure 3.1 illustrates the concept of selecting the neighboring pixels, which gives a beam of a theoretical width of about 1 px. The simulated beam shows aliasing artifacts as it not completely straight. Over many pixels however these effects cancel out and the simulation yields usable results.
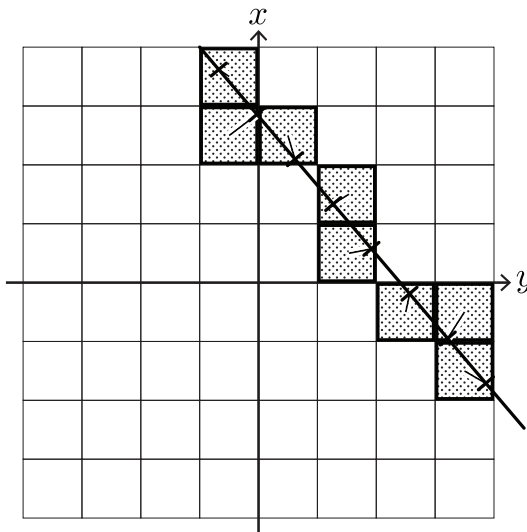
Figure 3.1: Simulation of a beam path

This summation over attenuation coefficients μ has its physical justification in Beer's Law (1.1), as the signal is transformed (see section 2.4) by

$$p_\gamma(\xi) = \ln\left(\frac{I_0}{I_\gamma(\xi)}\right).$$
(3.1)

20

If one then assumes two passes through pixels of beam length η_1, η_2 with attenuation coefficient μ_1, μ_2 behind each other in the path of the beam, this gives an intensity of

$$I = I_0 \cdot e^{-\mu_1 \eta_1} \cdot e^{-\mu_2 \eta_2} = I_0 \cdot e^{-(\mu_1 \eta_1 + \mu_2 \eta_2)} \tag{3.2}$$

and in turn a projection of

$$p = \ln \left(\frac{I_0}{I_0 \cdot e^{-(\mu_1 \eta_1 + \mu_2 \eta_2)}} \right) = \ln e^{\mu_1 \eta_1 + \mu_2 \eta_2} = \mu_1 \eta_1 + \mu_2 \eta_2. \tag{3.3}$$

After creating these data points they are stored in a file in a CSV-format, which is then opened by the imaging algorithm and processed into the reconstructed image. For the measured data the values have to be adapted as described in section 2.4.

Simulation results

Starting out with simple forms (figure 3.2) the back projection worked reasonably well, so errors were added to the simulation. In figure 3.2 (c) every value is distorted. The angle was disturbed by ± 2, the translation by $\pm 2\,\mathrm{mm}$ and the intensity by $\pm 5\,\%$ by modifying the values by a random amount within these ranges. This of course does not reflect the real world statistical error (which has a Gaussian distribution) but was sufficient for testing purposes. The image appears highly distorted while still remaining recognizable as the form in the input image.

(a) Input data   **(b)** Reconstructed image   **(c)** Reconstructed image with introduced error
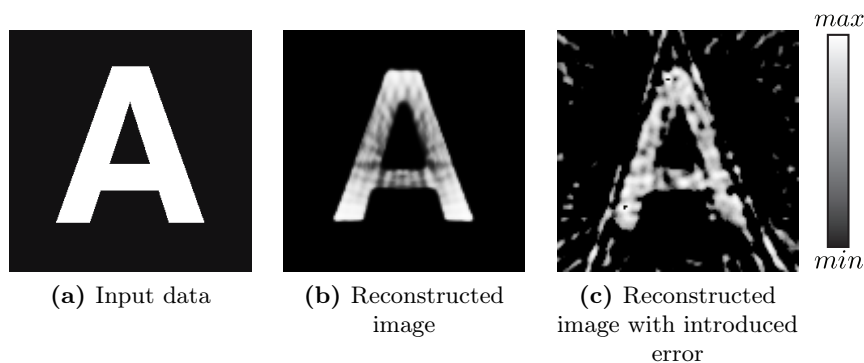
Figure 3.2: Simulation using the letter 'A'

The capacity of the reconstruction algorithm to resolve small structures was tested (see figure 3.3), with errors about half as great as the previously discussed simulation and comparable to the estimated errors in the real world. Being able to discriminate points of a size of down to at least $1.5\,\mathrm{mm}$, this is not a bottle neck in the ability of the

(a) Input data   **(b)** Reconstructed image   **(c)** Reconstructed image with introduced error
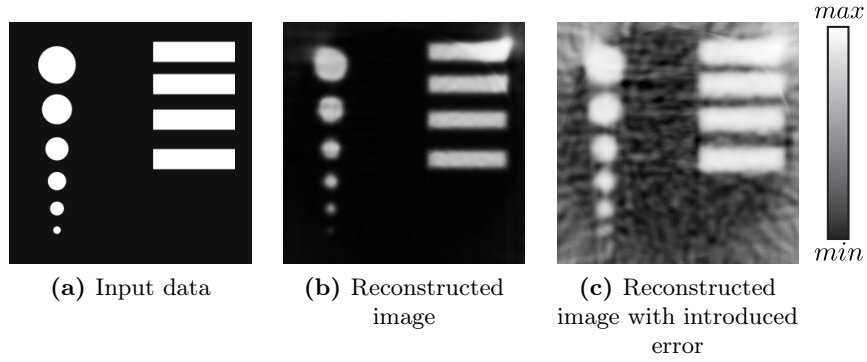
Figure 3.3: Simulation to test the expected resolving capacity of the algorithm with the number of data points obtained by real measurements

experiment to reproduce images as the smallest distance between two measured rays is about $1\,\mathrm{mm}$.

Different k-values

When using different values of k in the filter (1.20), for higher values of k the contrast increases, but the artefacts also become more noticeable (figure 3.4).

(a) $k = 1.0$ **(b)** $k = 1.1$ **(c)** $k = 1.2$ **(d)** $k = 1.3$ **(e)** $k = 1.4$ **(f)** $k = 1.5$
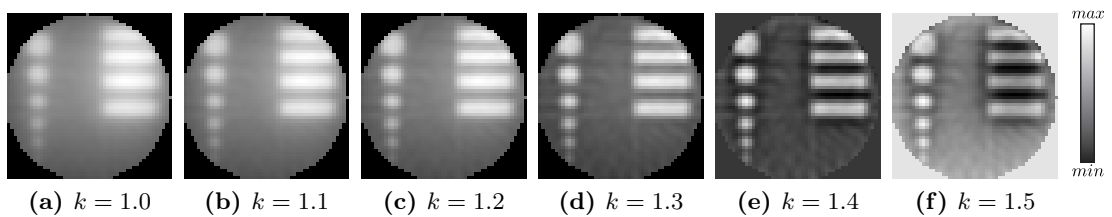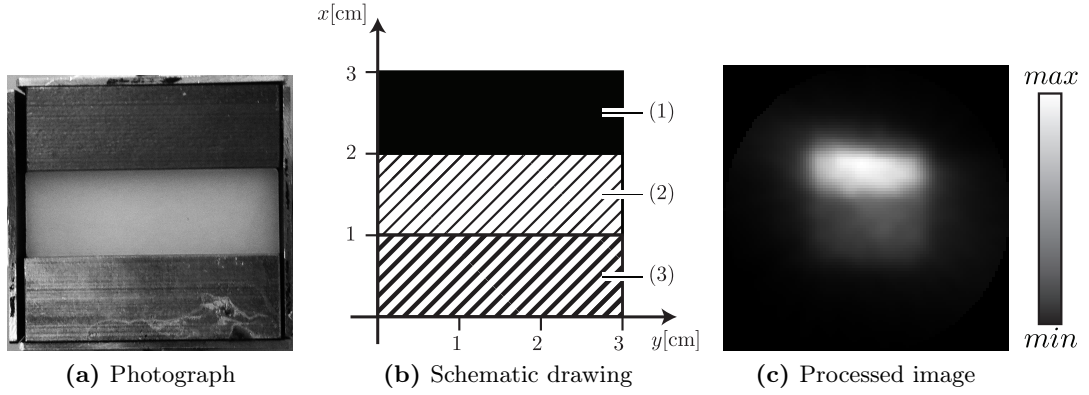
Figure 3.4: Simulation of different values of the filter constant k

As a compromise between those two aspects a value of $k = 1.2$ is used for the reconstruction of the real measurements. Figure 3.5 illustrates the filter function for different values of k.
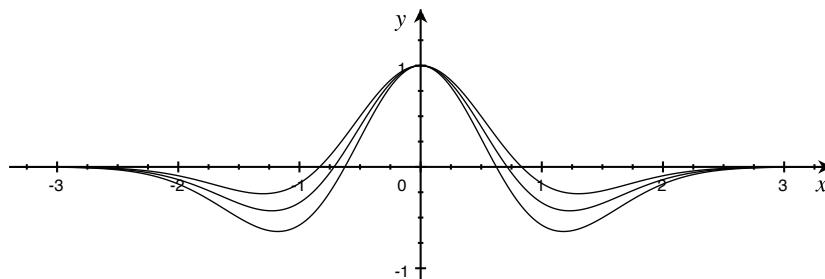
**Figure 3.5:** Filter with $k = \{1.2,\ 1.4,\ 1.6\}$

4 Measurements

(a) Photograph **(b)** Schematic drawing **(c)** Processed image

Figure 4.1: First long-term measurement

The first measurement was conducted collecting 30×30 data points using $60\,$s intervals. The sample consisted of three layers of material, each of which with dimensions of 3cm $\times$ 3cm $\times$ 1cm, using (1) iron ($\mu_{\text{Fe, 600 keV}} = 0.607\,$1/cm, [NIS95]), (2) Delrin/polyoxymethylene ($\mu_{(\text{CH}_2\text{O})_n,\text{ 600 keV}} = 0.1204\,$1/cm, [BHS$^+$10]) and (3) aluminum ($\mu_{\text{Al, 600 keV}} = 0.211\,$1/cm, [NIS95]).

The results can be seen in figure 4.1. While the layer of iron can be easily distinguished from the other layers, the other two layers can not be differentiated. This is surprising as the attenuation coefficients of Delrin and aluminum differ by a factor of about 2. This could be because of the short time and to few data points. Therefore the measure time was increased from $60\,$s to $120\,$s and the amount of data points from 900 to 1600 and later 2500.

(a) Photograph **(b)** Schematic drawing **(c)** Processed image
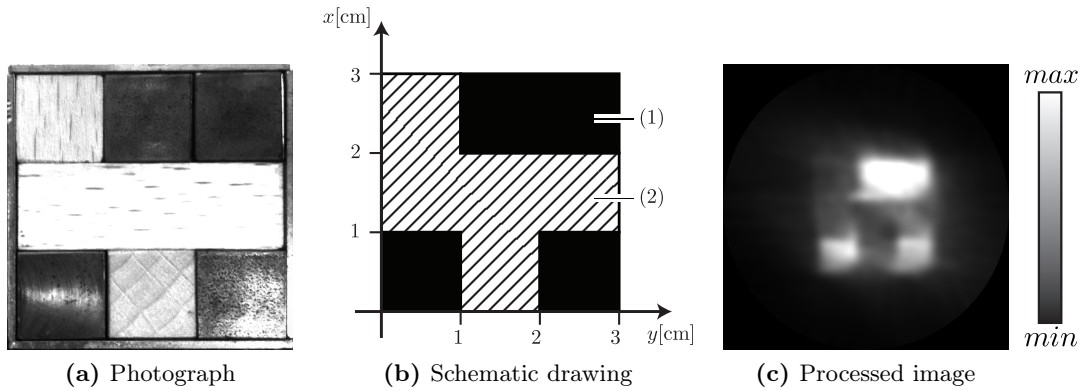
Figure 4.2: Second long-term measurement

For a second longer term measurement (figure 4.2) a pattern of 9 cubes of size $1\text{cm} \times 1\text{cm} \times 1\text{cm}$ was built. Four of the blocks are made of (1) iron and arranged in a pattern as to on the one hand easily confirm the orientation and on the other to rule out symmetrical artifacts. The empty spots were filled up with (2) woodblocks as they were of the lightest available material.
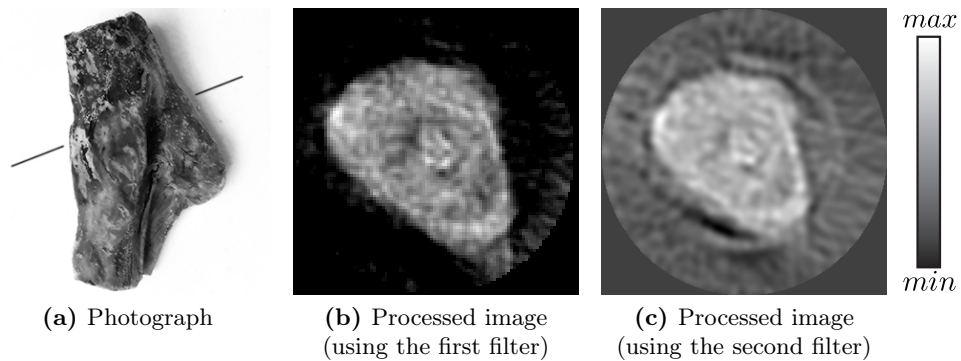
40×40 data points were taken (as was the original goal) using $120\,\text{s}$ intervals. The result of this measurement is displayed in figure 4.2. While some artefacts still remain the cubes are resolved very accurately and even the position of the wooden blocks can be easily determined, which poses a great improvement over the first measurement.

To test the reconstruction of small structures, a sample was built with rods of widths of 1-4 mm and scanned with 50×50 data points using $120\,\text{s}$ intervals. Even the rod with a diameter of only $1\,\text{mm}$ can be resolved.

(a) Photograph   (b) Schematic drawing   (c) Processed image
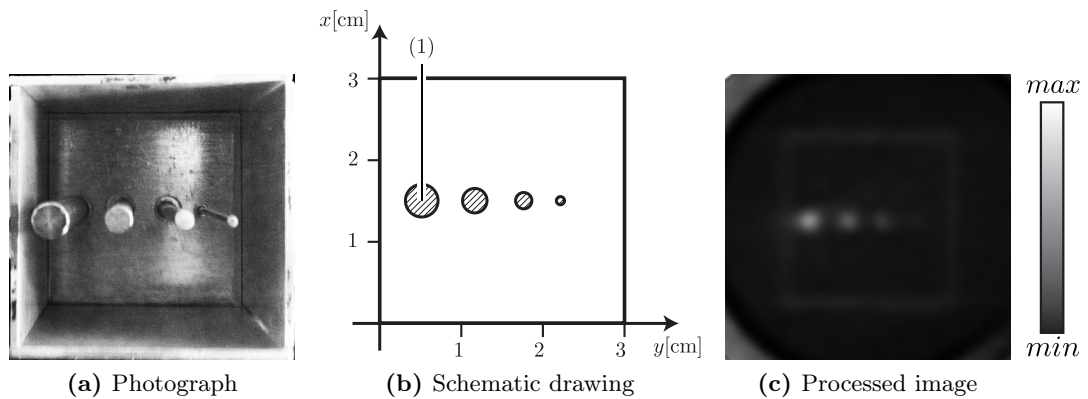
Figure 4.3: Measurement to determine the resolution capacity

Lastly the capability of resolving organic samples was tested by scanning a leg of a lamb (figure 4.4). 50×50 data points were taken using $120\,\text{s}$ intervals.

(a) Photograph   (b) Processed image (using the first filter)   (c) Processed image (using the second filter)

Figure 4.4: Measurement of the leg of a lamb

5 Conclusions and outlook

Results of the measurements

This experiment has proven to largely be a success, as in effect a custom CT apparatus was built from scratch that has a satisfactory resolution. It was possible to resolve structures of a size of 1 mm. This is a huge step from the original experiment mentioned in the introduction, which can not resolve blocks of size 1 cm reliably.

The increment of data points from 900 to 1600 and ultimately to 2500 provided a significant improvement in the resolution of the image with every step.

For the image reconstruction a lot of calculations a required as a lot of data and image points are processed. The computational time goes with $\mathcal{O}(N)$ for the resolution of the measurement in each direction and the image resolution in each direction. So for 40×40 measurement and a $100\,\mathrm{px} \times 100\,\mathrm{px}$ output image $40 \times 40 \times 100 \times 100 = 16.000.000$ projections and filter values are computed. Without the advent of widely available computers equipped with the computational power this experiment would have been unthinkable.

Improvement of the experiment

The mechanical implementation of the experiment is primarily made from Lego technic parts and lacks the desirable precision and rigidity (e.g. the rods connecting the gears have a very low torsional stiffness). An interesting expansion of the set-up would be the use of a detector array, allowing for shorter series of measurements and the use of stepper motors with continuous $360\,^\circ$ rotation enabling a better transmission and thereby greater precision.

The filtering function is empirical as described earlier and could certainly be refined, but the results were already found to be useful.

To achieve quantitative results it would be necessary to calibrate the set-up in terms of known attenuation of materials as well as an exact length scale.

Educational considerations

For this experiment to be suitable as a student experiment a few things have to be considered.

Firstly the experiment has to be understood by the student from a technical and theoretical as well as well as a user standpoint. This work and the work by O. Lemke [Lem14] aim to provide insight into various aspects of these scopes. While this thesis might be more suitable for getting a grasp on the theoretical foundations, practical directions for the usage of the involved software and its parameters are given in Lemkes work.

Secondly the experimental apparatus has to be built much more sturdily than it is now. With a lot of caution and care the experiment is able to function as shown before, but can be optimized both in terms of stability as well as durability (some parts broke several times). The lego parts are a very capable option for the fast creation of prototypes, but after the proof of feasibility, the mechanical parts should be made of a more solid material and manufactured more precisely.

Lastly the set-up of the apparatus and the software must be restructured and cleaned up to make for a more obvious structure and work.

While this experiment is largely automated, there are still many thinkable assignments to be done. There can be different samples to be scanned, as well as giving students the option to decide on their own objects. Some parameters need to be chosen (reasonable number of data points, meaningful measurement times ...) and can be varied.

We think one immensely educational task would be the development of a custom filter implementation, as it on the one hand very simple and offers direct visual feedback, but on the other hand teaches knowledge not only about the experiment itself and the nature of the filtered back projection but is also instructional for learning a little bit about programming.

Bibliography

[Ard14]   ARDUINO: *Arduino Uno.* `http://arduino.cc/en/Main/ArduinoBoardUno`. Version: 2014

[Bec06]   BECKMANN, E.C.: CT scanning the early days. *The British Journal of Radiology* 79 (206)

[BHS⁺10]   BERGER, M. J. ; HUBBELL, J. H. ; SELTZER, S. M. ; CHANG, J. ; COURSEY, J. S. ; SUKUMAR, R. ; ZUCKER, D. S. ; OLSEN, K.: *XCOM: Photon Cross Section Database (version 1.5).* `http://physics.nist.gov/xcom`. Version: 2010

[Buz08]   BUZUG, Thorsten M.: *Computed Tomography - From Photon Statistics to Modern Cone-Beam CT.* Berlin, Heidelberg : Springer, 2008. – ISBN 978–3–540–39408–2

[Dem05]   DEMTRÖDER, Wolfgang: *Experimentalphysik 3 - Atome, Moleküle und Festkörper.* Berlin : Springer DE, 2005. – ISBN 978–3–540–21473–1

[Dem10]   DEMTRÖDER, Wolfgang: *Experimentalphysik 4 - Kern-, Teilchen- und Astrophysik.* Berlin, Heidelberg : Springer, 2010. – ISBN 978–3–642–01598–4

[Dös99]   DÖSSEL, Olaf: *Bildgebende Verfahren in der Medizin - Von der Technik zur medizinischen Anwendung.* Berlin, Heidelberg : Springer, 1999. – ISBN 978–3–540–66014–9

[Gup12]   GUPTA, S. V.: *Measurement Uncertainties - Physical Parameters and Calibration of Instruments.* Berlin, Heidelberg : Springer, 2012. – ISBN 978–3–642–20989–5

[Klo07]   KLOSE, Prof. Dr. K. J.: *Einführung in die Radiologie - Anatomie in der Bildgebung.* 2007

[Lem14]   LEMKE, O.: *Computed Tomography - First generation CT for educational purposes*, Technische Universität Dortmund, Bachelorarbeit, 2014

[NIS95]   NIST ; NATIONAL INSTITUTE OF STANDARDS AND TECHNOLOGY (Hrsg.): *Tables of X-Ray Mass Attenuation Coefficients and Mass Energy-Absorption*

Coefficients from 1 keV to 20 MeV for Elements Z = 1 to 92 and 48 Additional Substances of Dosimetric Interest. National Institute of Standards and Technology, May 1995. `http://www.nist.gov/pml/data/xraycoef/index.cfm`

[Rad17] RADON, J.: Über die Bestimmung von Funktionen durch ihre Integralwerte längs gewisser Mannigfaltigkeiten. *Berichte über die Verhandlungen der Königlich Sächsischen Gesellschaft der Wissenschaften zu Leipzig. Mathematisch-Physische Klasse* 69 (1917), Nr. 262 - 277

[UHSC] UNTERWEGER, M.P. ; HOPPES, D.D. ; SCHIMA, F.J. ; COURSEY, J.S.: *Radionuclide Half-Life Measurements.* – URL: `http://www.nist.gov/pml/data/halflife-html.cfm`, viewed on Jan 22nd 2014

List of Figures

Appendices

A Arduino source code

The code for the control of the measurements and the mechanical components running on the Arduino board is printed here to demonstrate how straightforward the process of controlling the electronics is using the libraries provided by the Processing and Arduino language environments, that are based on the programming language Java.

Listing A.1: The Arduino source code

```
1   #include <Servo.h>
2
3   Servo myservo1;
4   Servo myservo2;
5   // create servo objects
6
7   int sensorPin = A3;
8   int measureTime = 120;
9   int trans_Steps = 40;
10  int rot_Steps = 40;
11  int offset = 20;
12  int offset_r = 0;
13  int x = 0;
14  int angle = 0;
15  int sensorValue = 0;
16  int oldSensorValue = 0;
17  long time = 0;
18  long currentCount = 0;
19  int cutOff = 400;
20
21  void setup()
22  {
23    myservo1.attach(9);
24    myservo2.attach(10);
25    // attaches the servos:
26    // rotation - Pin 09 (0-180), translation - Pin 10 (0-180)
27    Serial.begin(9600);
28  }
29
30  void loop() {
31    for (int trans_Step=0;trans_Step<trans_Steps;trans_Step
          ↪ +=1) {
32      x = int(1.0* trans_Step * ( (180-offset)/trans_Steps));
33      if (x<180-offset) {
34        delay(1000);
35        myservo2.write(x+offset);
36        myservo1.write(0);
37        delay(1000);
```

```
38        myservo2.write(x);
39        delay(1000);
40      }
41    for (int rot_Step=0; rot_Step<rot_Steps; rot_Step+=1) {
42        angle = int(float(rot_Step)*(((180.0-float(offset_r)))
            ↪ /float(rot_Steps)));
43        if (angle<180-offset_r) {
44          myservo1.write(angle+offset_r);
45          delay(500);
46          myservo1.write(angle);
47          delay(1000);
48        }
49        // === Measurement ===
50        currentCount=0;
51        time = millis();
52        while (millis()<time+measureTime*1000){
53          oldSensorValue = sensorValue;
54          sensorValue = analogRead(sensorPin);
55          if (sensorValue>cutOff && oldSensorValue<cutOff){
56            // positive slope triggering
57            currentCount+=1;
58          }
59        }
60        Serial.print(x);
61        delay(100);
62        Serial.print(",");
63        Serial.print(angle);
64        delay(100);
65        Serial.print(",");
66        Serial.println(int((currentCount*60.0)/float(
            ↪ measureTime)));
67        delay(100);
68
69      }
70    }
71  }
```
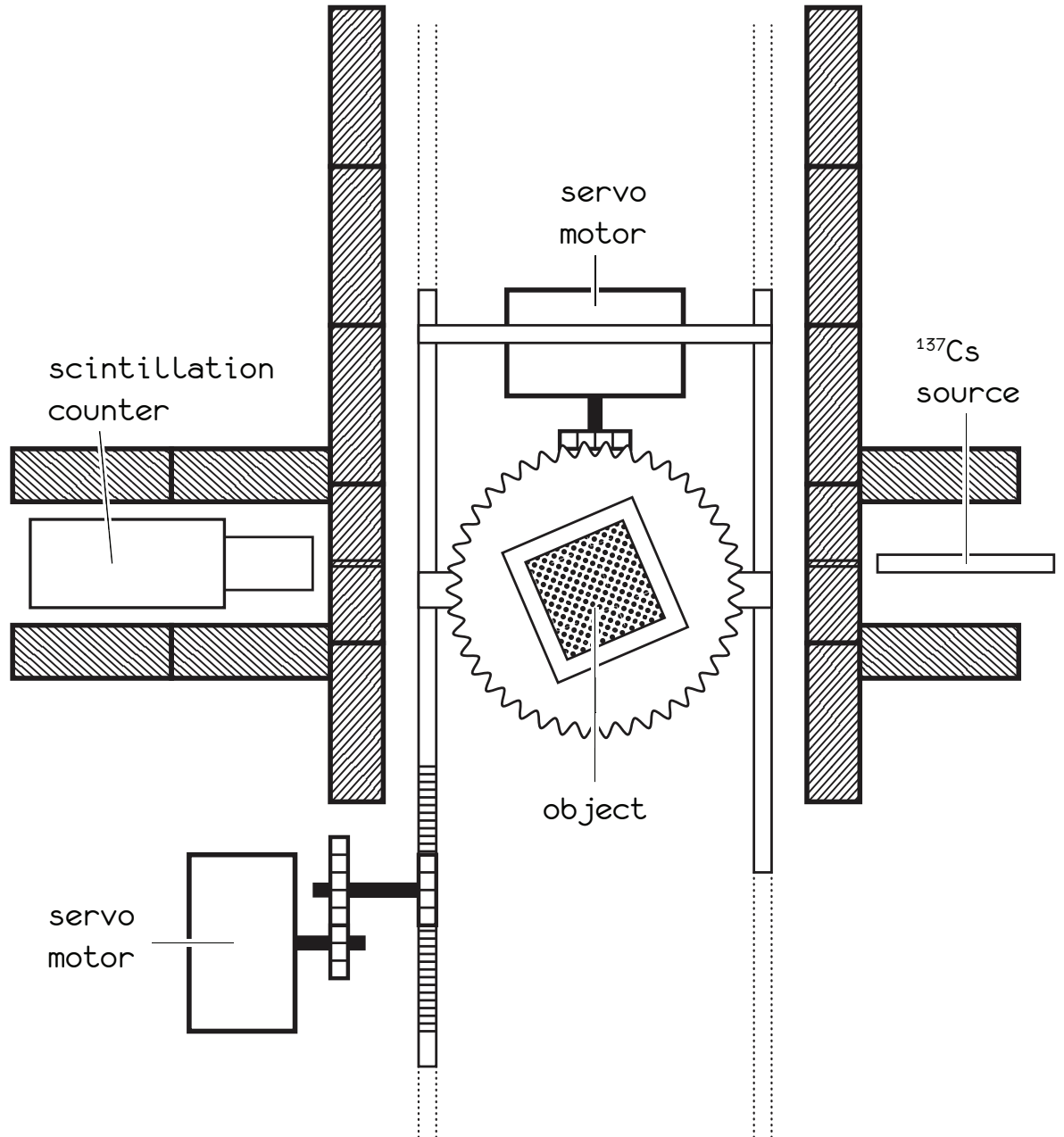
B Set-Up

Figure B.1: Set-up of the experiment

Eidesstattliche Versicherung

Ich versichere hiermit an Eides statt, dass ich die vorliegende Bachelorarbeit mit dem Titel "Computed tomography with gamma radiation and Arduino microcontrollers" selbständig und ohne unzulässige fremde Hilfe erbracht habe. Ich habe keine anderen als die angegebenen Quellen und Hilfsmittel benutzt sowie wörtliche und sinngemäße Zitate kenntlich gemacht. Die Arbeit hat in gleicher oder ähnlicher Form noch keiner Prüfungsbehörde vorgelegen.

_____ _____

Ort, Datum   Unterschrift